



# TiO<sub>2-x</sub>/CoO<sub>x</sub> photocatalyst sparkles in photothermocatalytic reduction of CO<sub>2</sub> with H<sub>2</sub>O steam



Yingying Li<sup>a</sup>, Changhua Wang<sup>a,\*</sup>, Miao Song<sup>b</sup>, Dongsheng Li<sup>b</sup>, Xintong Zhang<sup>a,\*</sup>, Yichun Liu<sup>a</sup>

<sup>a</sup> Key Laboratory for UV-Emitting Materials and Technology of Ministry of Education, Northeast Normal University, Changchun 130024, China

<sup>b</sup> Physical and Computational Sciences Directorate, Pacific Northwest National Laboratory, Richland, WA, 99352, United States

## ARTICLE INFO

### Keywords:

Photothermocatalysis  
CO<sub>2</sub> reduction  
Oxygen vacancies  
CoO<sub>x</sub>  
Solar fuel

## ABSTRACT

Solar photocatalytic production of fuels from CO<sub>2</sub> and H<sub>2</sub>O remains a challenging goal. Herein we report a strategy to co-modify TiO<sub>2</sub> with oxygen vacancies and CoO<sub>x</sub> nanoclusters for enhanced photothermocatalytic reduction of CO<sub>2</sub>. The TiO<sub>2-x</sub>/CoO<sub>x</sub> material exhibits prominently enhanced activity for the yield of CH<sub>4</sub> and CO under ultraviolet irradiation at elevated temperature of 393 K, which is 111.3- and 13.2-times greater yield of CH<sub>4</sub> and CO, respectively than the conventional photocatalytic process at 298 K, and 175.1- and 2.9-times greater yield of CH<sub>4</sub> and CO, respectively than the pristine TiO<sub>2</sub> under the same photothermocatalytic conditions. Control experiments over singly modified TiO<sub>2</sub> and doubly modified TiO<sub>2</sub> by different preparation history, together with high-resolution transmission electron microscope (HRTEM), electron spin resonance (ESR), and transient photovoltage measurements reveal the synergistic effect of oxygen vacancies and surface-grafted CoO<sub>x</sub> on the photothermocatalytic reduction of CO<sub>2</sub> to CH<sub>4</sub>, i.e. oxygen vacancies at TiO<sub>2</sub> surface facilitate the adsorption and reduction of CO<sub>2</sub> and the dispersion of CoO<sub>x</sub> nanoclusters, whereas surface-grafted CoO<sub>x</sub> clusters facilitate the hole trapping and the oxidation of H<sub>2</sub>O. Thereby the coexistence of oxygen vacancies and CoO<sub>x</sub> nanoclusters at TiO<sub>2</sub> surface promote the separation of photogenerated electrons and holes, and remarkably enhance the eight-electron reduction of CO<sub>2</sub> to CH<sub>4</sub> under photothermocatalytic conditions. This study shows the great potential of photo-thermal synergy on CO<sub>2</sub> reduction and provides a promising means to design photothermocatalysts for solar photocatalytic reduction of CO<sub>2</sub> to fuel.

## 1. Introduction

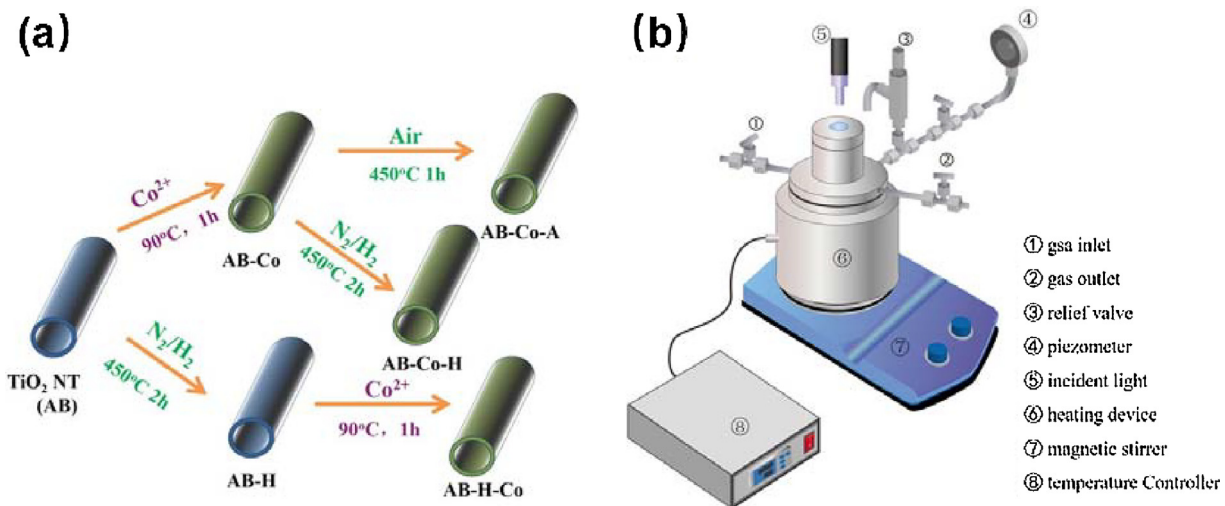
Artificial photosynthesis, which involves water splitting and CO<sub>2</sub> reduction processes inspired by natural photosynthesis, has attracted increasing interest for sustainable fuel production [1–4]. However, artificial photosynthesis by the above two processes is still challenged by low conversion efficiency and low selectivity of products [5–7]. Recent research has shown great promise of photo-thermal synergy for the catalytic reduction of CO<sub>2</sub>, by which a catalyst can exhibit activity for CO<sub>2</sub> reduction far exceeding the sum of photocatalytic activity and thermocatalytic activity in a photothermocatalytic process [8–12]. From a viewpoint of chemical thermodynamics [13], coupling photo-excitation with heating can favor the artificial photosynthesis by the following advantages: (1) heating helps the CO<sub>2</sub> reduction proceed because of an endothermic reaction; (2) heating water above 373 K converts liquid to gas whereby gaseous H<sub>2</sub>O and CO<sub>2</sub> are uniformly mixed, overcoming the normally low solubility of CO<sub>2</sub> in H<sub>2</sub>O; and (3) heating particularly accelerates the rate of reaction with a larger

activation energy according to Arrhenius equation, i.e. the water oxidation reaction in the case of artificial photosynthesis [14]. In these regards, it is in urgent demand to develop photothermocatalysts to tackle the low conversion efficiency and low selectivity issues of artificial photosynthesis.

Inorganic semiconducting materials are workhorse for photocatalytic reduction of CO<sub>2</sub> with H<sub>2</sub>O, of which conversion efficiency and selectivity are dependent on the capability of light absorption, charge separation and charge transfer pathways at the surface [15–18]. The semiconducting photocatalyst is often loaded with nanosized co-catalysts to enhance charge separation and modulate the reaction pathways of CO<sub>2</sub> reduction and water oxidation [19–22]. A number of studies focus on noble metal cocatalyst to promote CO<sub>2</sub> reduction reaction via electron transfer [23–25]. However, under the premise of CO<sub>2</sub> reduction with H<sub>2</sub>O, the hole transfer is no less important than electron transfer [20,26]. MO<sub>x</sub> (M = transition metal) nanoclusters are also frequently employed as co-catalysts either for electron or hole transfer dependent on composition [27–31]. Yamakata et al. studied the

\* Corresponding authors.

E-mail addresses: [wangch100@nenu.edu.cn](mailto:wangch100@nenu.edu.cn) (C. Wang), [xtzhang@nenu.edu.cn](mailto:xtzhang@nenu.edu.cn) (X. Zhang).



**Scheme 1.** (a): The synthetic process of catalysts; (b): Schematic diagram of reaction device.

behavior of photogenerated charge carriers over CoO<sub>x</sub>/LaTiO<sub>2</sub>N by time-resolved visible to mid-infrared absorption and compared with that of Pt/LaTiO<sub>2</sub>N [32]. They observed that holes were captured rapidly by CoO<sub>x</sub> in a few picoseconds and whereas electrons transfer by Pt proceeded over 0–100 μs, demonstrating the better role of CoO<sub>x</sub> cocatalysts for hole transfer. In fact, many reports have described effective CoO<sub>x</sub> cocatalyst for boosting water oxidation, including BiVO<sub>4</sub>, TaON, WO<sub>3</sub>, and TiO<sub>2</sub> supports [19,33–36]. Thus, CoO<sub>x</sub> cocatalyst deserves further investigation on CO<sub>2</sub> reduction with H<sub>2</sub>O. In particular, photothermocatalysis process is more complicated than that of photocatalysis, and additional photo-thermal synergy should be considered and closely correlated with behaviors of charge carriers over CoO<sub>x</sub> cocatalyst.

Another tough issue about artificial photosynthesis is the activation of CO<sub>2</sub> [37]. Recent study by Dong et al. [38] highlights that cocatalyst shows a prominent size effect for both activity and selectivity in CO<sub>2</sub> reduction. They revealed that smaller Pt nanoparticles showed superior performance in both CO<sub>2</sub> reduction and H<sub>2</sub> evolution because of promoted charge transfer efficiency; and whereas larger Pt nanoparticles showed a higher CH<sub>4</sub> selectivity because of higher proportion of surface terrace sites. On the other hand, recent theoretical calculations and experiments have proven that the introduction of oxygen vacancies onto TiO<sub>2</sub> decreases the energy of CO<sub>2</sub> adsorption and activation [39,40]. Further, the oxygen vacancies tend to strongly interact with surface-grafted MO<sub>x</sub> clusters [30,40,41]. This ensures ultra-dispersion of surface MO<sub>x</sub> cocatalyst and decreasing the size of cocatalyst. Thus, it is expected that a combination or even the synergy of oxygen vacancy and surface MO<sub>x</sub> cocatalyst can efficiently activate the TiO<sub>2</sub> for photothermocatalytic reduction of CO<sub>2</sub>. Herein, we propose a strategy that combines hydrogen treatment and CoCl<sub>2</sub> impregnation to co-modify the TiO<sub>2</sub> support. The anatase/TiO<sub>2</sub>(B) nanotube was selected as support because of its high surface area for ultra-dispersion of cocatalyst. This promotes charge separation at the interface of anatase/TiO<sub>2</sub>(B) [42]. CoO<sub>x</sub> nanoparticles were formed by hydrolysis of CoCl<sub>2</sub> on the surface of TiO<sub>2</sub> and their size could be varied by varying modification process. Structural characterization reveals that a TiO<sub>2-x</sub>/CoO<sub>x</sub> catalyst is achieved in which CoO<sub>x</sub> nanoparticles with a diameter below 2 nm offer a surprising activity for CH<sub>4</sub> production. This yield can be 175 times higher than that of pristine TiO<sub>2</sub>, which indeed confirms a significant photothermal synergy. The reasons for the high activity of TiO<sub>2-x</sub>/CoO<sub>x</sub> photothermocatalyst are systematically understood via capture of CO<sub>2</sub> at oxygen vacancy, dual charge separation by oxygen vacancy and CoO<sub>x</sub> cocatalyst, and multiple electron/proton accumulation at the interface of TiO<sub>2-x</sub>/CoO<sub>x</sub>.

## 2. Experimental section

### 2.1. Synthesis of samples

The synthesis of TiO<sub>2</sub> and CoO<sub>x</sub> modified TiO<sub>2</sub>: TiO<sub>2</sub> support was synthesized by a method reported previously [42]. The nanotubes composed of anatase and TiO<sub>2</sub>(B) were obtained by calcination at 450 °C for 2 h. For simplicity, TiO<sub>2</sub> sample with anatase and TiO<sub>2</sub>(B) was named AB. A simple impregnation was employed to graft CoO<sub>x</sub> nanoparticles on TiO<sub>2</sub>(AB) nanotubes. The 0.5 g TiO<sub>2</sub>(AB) was dispersed in 10 ml of deionized water, followed by 5 mL of CoCl<sub>2</sub> (CoCl<sub>2</sub>·6H<sub>2</sub>O, Tianjin guangfu technology development Co. Ltd., 99.0%) solution (2.04 mM) to the suspension. The suspension was further stirred at 90 °C for 1 h. Finally, the as-obtained light green powders were centrifuged, washed with water, and dried at 110 °C for 24 h. For simplicity, this sample was named AB-Co. For comparison, AB-Co was calcined in air at 450 °C for 2 h and named AB-Co-A.

Synthesis of defective TiO<sub>2</sub> and grafting CoO<sub>x</sub> on defective TiO<sub>2</sub>: To introduce oxygen defects into TiO<sub>2</sub>, the AB sample was calcined at 450 °C for 2 h in N<sub>2</sub>/H<sub>2</sub>(9:1) mixture with a flow speed at 125 mL/min in the tube furnace, which is named AB-H.

The order of hydrogenation and CoO<sub>x</sub> grafting was considered when oxygen defects and CoO<sub>x</sub> were simultaneously integrated on TiO<sub>2</sub>. The two samples were named AB-H-Co and AB-Co-H. Here, AB-H-Co means AB sample modified by hydrogenation followed by CoO<sub>x</sub> grafting and AB-Co-H means AB sample modified by CoO<sub>x</sub> grafting, followed by hydrogenation. **Scheme 1a** illustrates the synthesis route of all samples.

Details about the characterization are described in the supporting information.

### 2.2. Photothermal reduction of CO<sub>2</sub>

Photothermal reduction of CO<sub>2</sub> used an autoclave (Anhui Kemi Machinery Technology Co., Ltd.) with a total volume of 100 ml. First, 0.05 g catalyst powders and 2 mL of deionized water were added to the autoclave. Then, the reactor was blown with CO<sub>2</sub> (99.999%) for 20 min to ensure that the reaction system was filled with pure carbon dioxide. Finally, the clave was sealed, heated to 393 K irradiated from the top with a 150 W UV lamp (Hayashi UV410). **Scheme 1b** illustrates the reaction device. The window area for light irradiation was 3 cm<sup>2</sup>, and the circular groove area for powder catalyst was 13.9 cm<sup>2</sup>, respectively. The light intensity irradiated on the samples was 20 mW/cm<sup>2</sup> at 365 nm. The generation of CO and CH<sub>4</sub> was monitored using a gas chromatograph (model GC-2014, Shimadzu Co., Ltd.). For comparison, a photocatalytic test was performed at room temperature and other

conditions remained the same as the photothermocatalytic test.

### 3. Results and discussion

We prepared anatase/TiO<sub>2</sub>(B) nanotubes (named AB) as reported in our previous work [42]. The lattice mismatch at the interface of anatase (101)/TiO<sub>2</sub>(B) (110) is 1.36% [43,44], which is much lower than the 7.76% mismatch at the anatase (101)/rutile (110) interface, suggesting a better suppression of charge recombination of anatase/TiO<sub>2</sub>(B) than anatase/rutile. Moreover, one dimensional AB nanotubes provide a better charge transport. The surface area of as-adopted AB nanotubes is as high as 277 m<sup>2</sup> g<sup>-1</sup>, which not only benefits the ultra-dispersion of CoO<sub>x</sub> cocatalyst, but it also offers many active sites for the catalytic conversion of CO<sub>2</sub>.

Photothermocatalysis is more complicated than photocatalysis and the synergy of photocatalysis and thermocatalysis should be considered. The well-known mechanisms in photocatalysis might not be applied to photothermocatalysis. In photocatalysis, the introduction of oxygen defects into the photocatalyst effectively boost the activity until a significant visible absorption of TiO<sub>2</sub> is observed [45]. In another word, slight oxygen defects lead to insignificant visible absorption that does not improve the photocatalytic activity. It is not clear if an inactive photocatalyst with slight oxygen defect leads to an inactive photothermocatalyst. On the other hand, the loading amount of MO<sub>x</sub> cocatalyst onto TiO<sub>2</sub> photocatalyst is usually 1–10 wt%. When the loading amount of cocatalyst is lower than 1 wt%, it is difficult to observe any activity enhancement. Thus, we wonder whether a photocatalyst with a cocatalyst lower than 1 wt% implies an inactive photothermocatalyst.

To address these gaps in knowledge, we intentionally introduced a slight oxygen vacancy and ultra-low amount of CoO<sub>x</sub> cocatalyst onto AB nanotubes. In photocatalysis, neither the introduction of slight oxygen vacancy nor the ultra-low amount of CoO<sub>x</sub> cocatalyst significantly enhances the photocatalytic activity. In spite of the slight modification, the strategy can significantly activate TiO<sub>2</sub> in photothermocatalysis. To clarify the superior performance of TiO<sub>2-x</sub>/CoO<sub>x</sub> in photothermocatalysis versus photocatalysis, we next focus on six typical samples of AB, AB-H, AB-Co, AB-Co-A, AB-Co-H, and AB-H-Co to demonstrate the contribution of each modification. By systematic comparison, the single role of oxygen vacancy, CoO<sub>x</sub> cocatalyst, as well as the synergy effect between oxygen vacancy and CoO<sub>x</sub> cocatalyst on the photothermocatalytic activity are studied.

#### 3.1. Ultra-dispersion of CoO<sub>x</sub> nanoparticles on AB nanotubes and further decrease of size on AB-H nanotubes

The morphological structures of samples were observed by SEM and TEM. As shown in Fig. 1a, AB sample takes on one-dimensional nanostructure feature. From the TEM pictures (Fig. 1b), it can be characterized nanotubes with a diameter of ca. 10 nm. There is no appreciable morphological change regardless of thermal treatment in air or N<sub>2</sub>/H<sub>2</sub> (Fig. S1-S2), indicating that AB nanotubes have a good thermal stability. In addition to the above AB and AB-H nanotubes, grafting CoO<sub>x</sub> species on AB nanotubes was performed under three cases. After grafting, the measured atomic percentage of Co in AB-Co-H, AB-Co, and AB-H-Co was 0.19 wt%, 0.19 wt% and 0.15 wt% indicated by ICP element analysis respectively, which is in accordance with the starting stoichiometric ratio (0.12 wt%) in the synthesis process. Theoretically, 0.12 wt% Co grafting corresponds to 0.046 Co atom per nm<sup>2</sup> by assuming that CoO<sub>x</sub> species are uniformly distributed on the surface of AB nanotube. Thus, the grafted CoO<sub>x</sub> species onto TiO<sub>2</sub> are supposed to be highly separated from each other and are ultra-small [46].

The HAADF image of the as-obtained AB-Co-H sample is acquired and shown in Fig. 1c. Bright nanoparticles are uniformly distributed around the dark nanotubes, confirming that CoO<sub>x</sub> nanoparticles were successfully grafted on the defective AB nanotubes. The HRTEM image (Fig. 1g) shows that the diameter of CoO<sub>x</sub> nanoparticles is ca. 5 nm. The

FFT pattern indicates that CoO<sub>x</sub> nanoparticles are crystallized into CoO nanocrystals, as shown in Fig. S3. FFT pattern of shedding nanoparticles from sample AB-Co-H is of hexagon shape. The spots and angles between spots can be well assigned to CoO along [124] zone axis. Element mapping was further conducted to determine the distribution of component elements. As can be seen and compared in Fig. 1d–f, elemental Co was uniformly distributed on the nanotubes. When AB nanotubes were only modified by CoO<sub>x</sub> nanoparticles, HRTEM image of AB-Co sample gives a diameter of CoO<sub>x</sub> nanoparticles ca. 2 nm, as shown in Fig. 1h. FFT pattern suggest that the CoO<sub>x</sub> nanoparticles are amorphous. The smaller diameter compared with that of AB-Co-H is believed to result from the aggregation of CoO<sub>x</sub> nanoparticles by the thermal treatment during hydrogenation of AB nanotubes. When the CoO<sub>x</sub> nanoparticles were grafted onto AB-H nanotubes, they are too small to be observed by HRTEM, as shown in Fig. 1i. The smallest CoO<sub>x</sub> nanoparticles among three CoO<sub>x</sub> grafted TiO<sub>2</sub> samples may benefit from strong interactions between oxygen vacancy defects and CoO<sub>x</sub> nanocluster, which will be discussed in detail via other characterization. Accordingly, it can be concluded that CoO<sub>x</sub> nanoparticles can be ultradispersed on AB nanotubes. The size of CoO<sub>x</sub> nanoparticles in these three samples ranges in the following order: AB-Co-H > AB-Co > AB-H-Co. The CoO<sub>x</sub> nanoparticles on AB-Co and AB-H-Co are amorphous whereas the CoO<sub>x</sub> nanoparticles on AB-Co-H are crystallized into CoO nanocrystals.

#### 3.2. Phase composition

X-ray diffraction (XRD) characterization was performed on the Si substrate to calibrate the position of the diffraction peaks of TiO<sub>2</sub> sample. After calibration, the diffraction pattern of AB (Fig. 2a) can be identified as mixed phases of anatase (JCPDS file no.21-1272) and TiO<sub>2</sub>(B) (JCPDS file no.46-1237). The modifications, including hydrogenation and CoO<sub>x</sub> grafting, lead to no change of original diffraction pattern, due to the slight oxygen vacancy and ultra-low amount of CoO<sub>x</sub>. Raman spectra (Fig. 2b) can provide further information on the phase composition and defects in TiO<sub>2</sub>. As shown in Fig. 2b, the bands at 144, 197, 399, 515, and 639 cm<sup>-1</sup> are corresponding to E<sub>g</sub>, E<sub>g</sub>, B<sub>1g</sub>, A<sub>1g</sub> + B<sub>1g</sub>, and E<sub>g</sub> modes of anatase [47]. The bands at 119.5 cm<sup>-1</sup> and 251.4 cm<sup>-1</sup> are assigned as TiO<sub>2</sub>(B) [48]. On close inspection of the E<sub>g</sub> band at 144 cm<sup>-1</sup> in AB-H and AB (Fig. 2c), we note a subtle shift to higher wavenumber after hydrogenation of AB nanotubes, which indicates the existence of structural disorders related to the oxygen vacancies in AB-H sample [49,50].

(c) Magnified Raman spectra of AB and AB-H in the regions of 133–155 cm<sup>-1</sup>.

#### 3.3. Analysis on local environment around grafted CoO<sub>x</sub> species

Fig. 3a displays the UV-vis spectra of different samples. In the region between 200 and 500 nm, CoO<sub>x</sub> grafting hardly change the absorption of AB nanotubes, which agrees with the ultra-low amount of CoO<sub>x</sub> nanoparticles. Meanwhile, hydrogenation results in only minor visible light absorption, indicating that a slight oxygen vacancy was introduced. There is also an absorption peak at 550–670 nm in the CoO<sub>x</sub> modified TiO<sub>2</sub> sample. As reported, d-d electron transition of Co<sup>2+</sup> gives a very similar absorption in the same region [51]. On recalling the aforementioned results of HRTEM image of AB-Co-H, the CoO<sub>x</sub> nanoparticles existed in terms of CoO crystal. Therefore, it is believed that the additional absorption at 550–670 nm in AB-Co-H originates from the d-d electron transition of octahedral Co<sup>2+</sup>. Since there is no obvious difference between the d-d electron transition-related absorption in all CoO<sub>x</sub> modified samples, it is deduced that the as-grafted CoO<sub>x</sub> species in all samples exist in the state of Co<sup>2+</sup>.

The bonding environment of elements in different samples is further analyzed by XPS. Note that no Co related XPS peaks appear over all CoO<sub>x</sub> modified samples (Fig. S5). This is because the amount of grafted

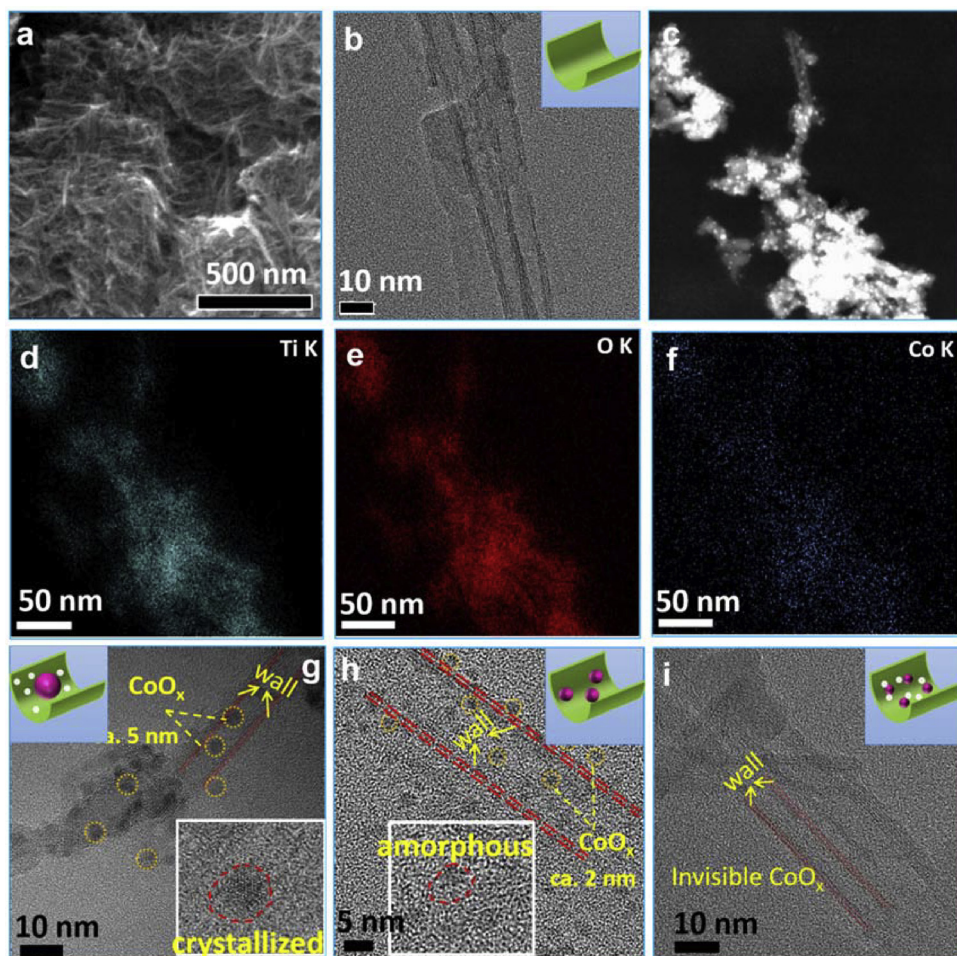


**Fig. 1.** (a) SEM image of AB; (b) TEM image of AB; (c) HAADF images and (d–f) EDS mappings of AB-H-Co; (g–i) HRTEM images of AB-Co-H, AB-Co, and AB-H-Co; insets are the models of the samples.

$\text{CoO}_x$  (0.15–0.19 wt%) is far lower than the detection limit of 0.6 wt% for Co element according to the precision of the instrument. Figs. 3b and 3c show the XPS peaks of Ti 2p and O 1s of all samples. For AB sample, there are two individual peaks at 458.47 eV and 464.17 eV, which can be indexed to Ti 2p<sub>3/2</sub> and Ti 2p<sub>1/2</sub> binding energy of  $\text{Ti}^{4+}$  state [52,53]. For samples AB-Co and AB-Co-A, the binding energy of the Ti 2p peaks exhibit a slight shift to higher value. This is related to the formation of Ti–O–Co bond via the surface bonding between Co and Ti, due to the higher electronegativity of Co than that of Ti [54–56]. In contrast, for AB-H sample, the peaks of Ti 2p and O 1s

slightly shift to lower BE, which is related to the introduction of oxygen vacancy defects via hydrogen treatment [57]. Samples AB-Co-H and AB-H-Co have little shift in the binding energy of Ti 2p and O1s likely because of a synergistic effect between the oxygen vacancy and the  $\text{CoO}_x$  grafting. However, it is noted that the peak of Ti 2p in AB-H-Co shifts to higher binding energy. In fact, as observed in the HRTEM images,  $\text{CoO}_x$  on AB-H-Co has a higher dispersion and smaller size than that on AB-Co-H. This indicates a stronger interaction between  $\text{CoO}_x$  and  $\text{TiO}_2$  in sample AB-H-Co. In view of positive shift of Ti 2p peak induced by  $\text{CoO}_x$  grafting, it is believed that higher binding energy of

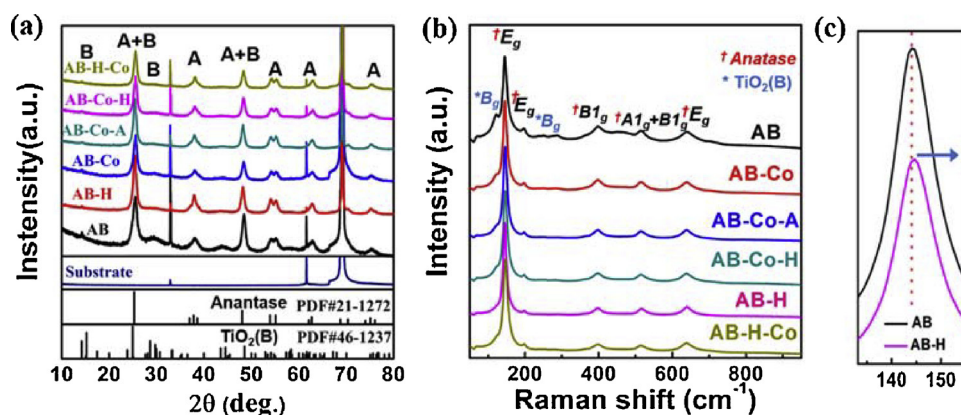


**Fig. 2.** (a) XRD patterns of different samples, (b) Raman spectra of different samples.

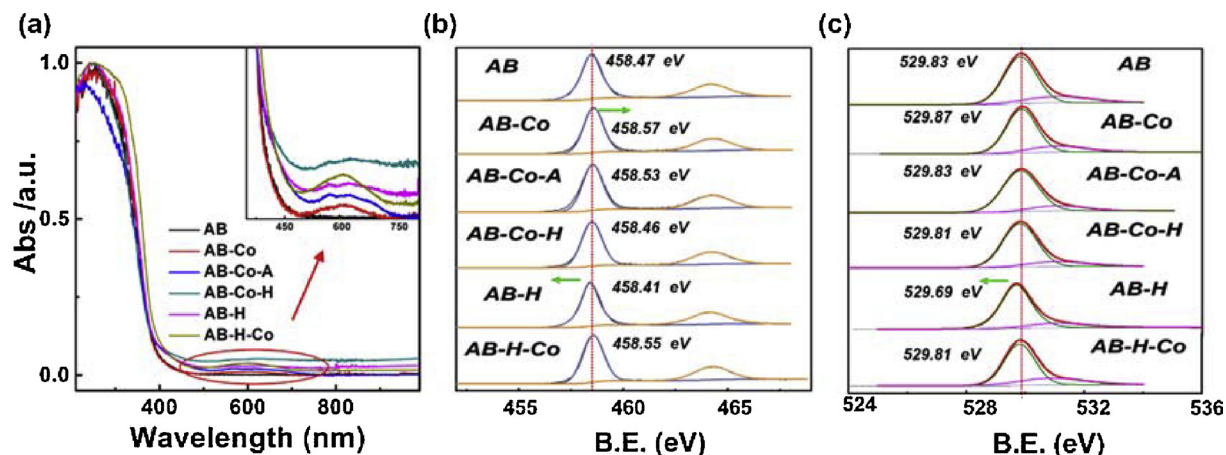


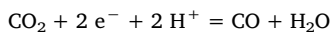
Fig. 3. (a) UV-vis spectra of different samples; (b) XPS spectra of Ti 2p and (c) O 1s core level of the as-prepared samples; all peak maxima were calibrated to C1 s at 284.6 eV.

Ti2p peak in AB-H-Co than AB-Co-H results from a better dispersion of  $\text{CoO}_x$  and stronger interaction between  $\text{CoO}_x$  and  $\text{TiO}_2$ .

### 3.4. The photothermal synergy in $\text{CO}_2$ reduction over AB-H-Co

Fig. 4 shows the results of catalytic reduction of  $\text{CO}_2$  over sample AB-H-Co. By photocatalysis, the production rate of CO and  $\text{CH}_4$  is 1.2473 and 0.0903  $\mu\text{mol/g/h}$ , respectively, indicating that CO is the main product. Surprisingly, by photothermocatalysis, massive CO and  $\text{CH}_4$  can be simultaneously produced. The production rates of CO and  $\text{CH}_4$  are enhanced by 13.2 and 111.3 times, respectively. From the compared results between photocatalysis and photothermocatalysis, there is a photo-thermal synergy over sample AB-H-Co for catalytic reduction of  $\text{CO}_2$ . The drastic enhancement of  $\text{CH}_4$  production is mainly due to the grafting of ultra-small  $\text{CoO}_x$  rather than the introduction of oxygen vacancy, which will be discussed in detail later. TOF value is calculated to be 0.4936  $\text{h}^{-1}$  according to the number of active sites of  $\text{CoO}_x$ . Assuming that CO and  $\text{CH}_4$  are the only products in photothermocatalysis, the apparent quantum efficiency at 365 nm is  $1.26 \times 10^{-2} \%$ .

In the catalytic reduction of  $\text{CO}_2$ , CO and  $\text{CH}_4$  are produced via the transfer of two and eight electrons, as shown in the following equation:



The catalytic activity can be quantitatively evaluated by N-electrons, which is calculated according to the following equation.

$$\text{N-electrons} = 2n(\text{CO}) + 8 n(\text{CH}_4),$$

where the  $n(\text{CO})$  and  $n(\text{CH}_4)$  mean consumption rate of electrons for production of CO and  $\text{CH}_4$ , respectively. The calculated values are listed in Table 1. Accordingly, sample AB-H-Co again gives a much higher value of N-electrons via photothermocatalysis than that by photocatalysis ( $681.8 \times 10^{17}$  vs  $19.4 \times 10^{17}$ ). This further confirms the photothermal synergy over sample AB-H-Co for the catalytic reduction of  $\text{CO}_2$ .

As is well reported,  $\text{H}_2\text{O}$  oxidation by photo-induced hole proceeds via two steps [58,59]. Firstly,  $\text{H}_2\text{O}$  is oxidized by hole to produce  $\text{H}^+$  ions and  $\text{OH}$  radical. Secondly,  $\text{H}_2\text{O}$  is oxidized by  $\text{OH}^-$  radicals and holes to produce  $\text{O}_2$  and  $\text{H}^+$ . We try to measure the amount of  $\text{O}_2$  over sample AB-H-Co, but no oxygen is detected. Herein, the missing of oxygen may be due to following factors: (1) consumption of  $\text{O}_2$  through the reaction with photogenerated electrons; (2) back reaction of  $\text{O}_2$  with  $\text{H}^+$  or  $\text{H}_2$  and (3) the low sensitivity of TCD for detection of trace  $\text{O}_2$  production.

#### 3.4.1. The photothermal synergy in $\text{CO}_2$ reduction over pristine AB

Fig. 5a shows the results of photocatalytic and photothermocatalytic reduction of  $\text{CO}_2$  over pristine AB. In our previous work and others' work, pure  $\text{TiO}_2$  was found inert at producing  $\text{CH}_4$  via photocatalytic reduction of  $\text{CO}_2$ , due to the limited onset of coupled multielectron-

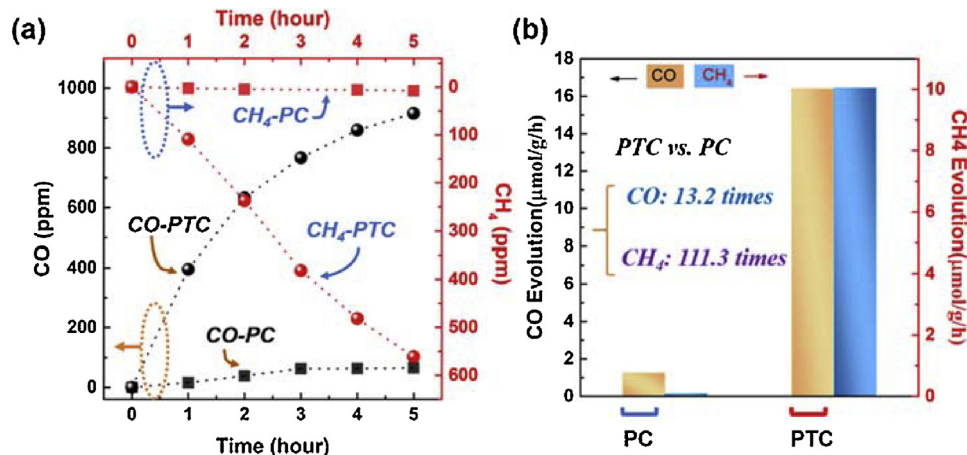


Fig. 4. (a) Time curves of CO and  $\text{CH}_4$  production and (b) amount of CO and  $\text{CH}_4$  formed in photocatalytic and photothermocatalytic  $\text{CO}_2$  conversion over AB-H-Co. PC stands for photocatalysis and PTC stands for photothermocatalysis.

**Table 1**

Catalytic activities of photocatalytic and photothermocatalytic induced  $\text{CO}_2$  conversion over different samples. a: Reaction conditions: room temperature, catalyst (0.05 g),  $I_{365} = 20 \text{ mW cm}^{-2}$ , 1.01 bar  $\text{CO}_2$ ; b: Reaction conditions:  $393 \pm 5 \text{ K}$ , catalyst (0.05 g),  $I_{365} = 20 \text{ mW cm}^{-2}$ , 1.33 bar  $\text{CO}_2$ ; c:  $\text{CO}$ -selectivity =  $2 \times (\text{CO-yield}) / [2 \times (\text{CO-yield}) + 8 \times (\text{CH}_4\text{-yield})]$ ; d:  $\text{CH}_4$ -selectivity =  $8 \times \text{CH}_4\text{-yield} / [2 \times (\text{CO-yield}) + 8 \times (\text{CH}_4\text{-yield})]$ .

Sample	Photocatalysis <sup>a</sup>					Photothermocatalysis <sup>b</sup>				
	CO-yield ( $\mu\text{mol/g/h}$ )	CO-selectivity <sup>c</sup>	CH <sub>4</sub> -yield ( $\mu\text{mol/g/h}$ )	CH <sub>4</sub> -selectivity <sup>d</sup>	N-electrons ( $10^{17}$ )	CO-yield ( $\mu\text{mol/g/h}$ )	CO-selectivity	CH <sub>4</sub> -yield ( $\mu\text{mol/g/h}$ )	CH <sub>4</sub> -selectivity	N-electrons ( $10^{17}$ )
AB	0.6819	100%	/	/	8.2128	5.6656	96.11%	0.0574	3.89%	71.0018
AB-Co	0.9019	80.82%	0.0535	19.18%	13.4399	10.240	47.70%	2.8066	52.30%	258.5413
AB-Co-A	0.5786	83.98%	0.0276	16.02%	8.2983	8.7806	67.42%	1.0609	32.58%	156.8635
AB-H	0.4934	68.09%	0.0578	31.91%	8.7271	13.362	87.37%	0.4829	12.63%	184.1961
AB-Co-H	0.8105	81.50%	0.0460	18.50%	11.978	11.021	88.33%	0.3640	11.67%	150.2730
AB-H-Co	1.2473	77.54%	0.0903	22.46%	19.4017	16.403	28.98%	10.051	71.02%	681.7747

multiproton transfer ( $8\text{e}^-/8\text{H}^+$ ) [60]. Thus, no  $\text{CH}_4$  is likewise produced, and the apparent quantum efficiency at 365 nm is as low as  $4.02 \times 10^{-4} \%$ . In photothermocatalysis, very little  $\text{CH}_4$  (0.05  $\mu\text{mol/g/h}$ ) is produced. However, there is a significant enhancement is observed in photothermocatalysis versus photocatalysis with regard to the production of  $\text{CO}$ . The  $\text{CO}$  production rate via photothermocatalysis is ca. 8.3 times higher than that of photocatalysis. Therefore, there is a photothermal synergy for enhanced production of  $\text{CO}$  versus  $\text{CH}_4$ .

### 3.4.2. The effect of the oxygen vacancies on the photothermal $\text{CO}_2$ reduction

To evaluate the influence of oxygen vacancy on photothermocatalytic reduction of  $\text{CO}_2$ , the catalytic activity of AB-H was tested and compared with AB. By photocatalysis, the AB-H is different from AB in that AB-H enables not only evolution of  $\text{CO}$  but also  $\text{CH}_4$  from  $\text{CO}_2$  reduction, as seen in Fig. 5b. Despite this, the activity

enhancement induced by oxygen vacancy via single photocatalysis is not striking. By photothermocatalysis, AB-H displays a more significantly enhanced production of  $\text{CO}$  and  $\text{CH}_4$ . The production rate of  $\text{CO}$  and  $\text{CH}_4$  over AB-H is 27 and 8-fold higher than that via photocatalysis. Therefore, it can be concluded that photothermocatalysis is more promising than photocatalysis in  $\text{CO}_2$  reduction, even introduction of a slight oxygen vacancy indeed results in a significantly enhanced production of  $\text{CO}$  and  $\text{CH}_4$ .

### 3.4.3. The effect of $\text{CoO}_x$ and its dispersion on the photothermal $\text{CO}_2$ reduction

Fig. 5c shows the results of photocatalytic and photothermocatalytic reduction of  $\text{CO}_2$  over AB-Co. By photocatalysis, the grafting of  $\text{CoO}_x$  leads to no obvious enhancement of  $\text{CO}$  and  $\text{CH}_4$  production, which is limited by the ultra-low amount of  $\text{CoO}_x$  nanoparticles. However, by photothermocatalysis, impressive yields of products are observed. For

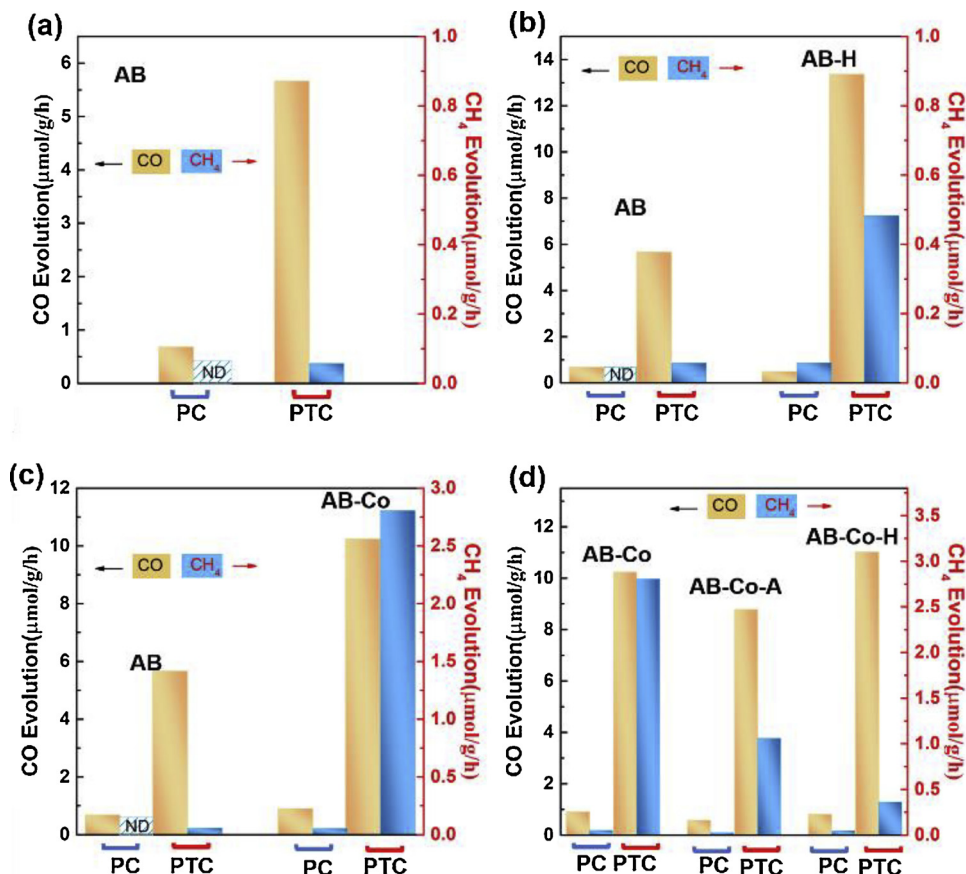


**Fig. 5.** Amount of  $\text{CO}$  and  $\text{CH}_4$  formed in photocatalytic and photothermocatalytic induced  $\text{CO}_2$  conversion over (a) AB; (b) AB and AB-H; (c) AB and AB-Co; and (d) AB-Co, AB-Co-A, and AB-Co-H. PC stands for photocatalysis and PTC stands for photothermocatalysis. ND = not detected.

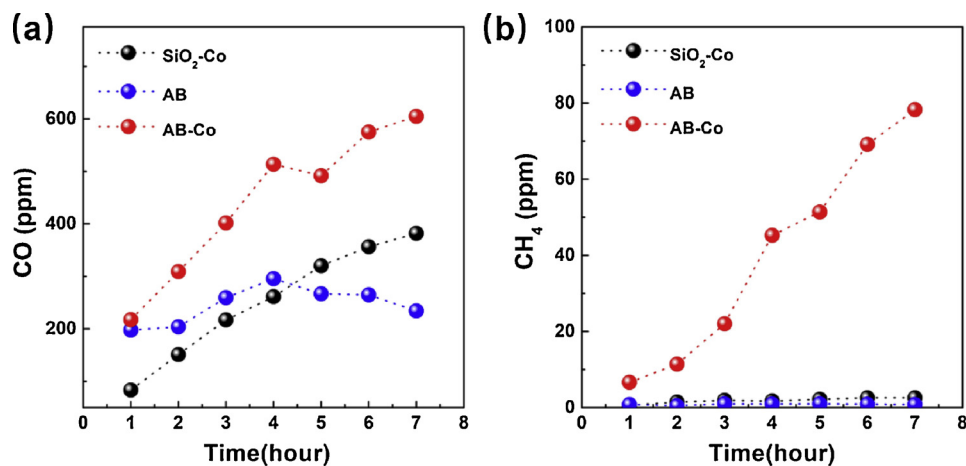


Fig. 6. Time curves of (a) CO and (b) CH<sub>4</sub> evolution in photothermocatalytic induced CO<sub>2</sub> conversion over AB, SiO<sub>2</sub>-Co, and AB-Co.

CO production, the production rate over AB-Co is 11.35 times higher than AB and comparable to AB-H. For CH<sub>4</sub> production, the production rate over AB-Co is drastically increased by 52.46 times and far higher than that of AB and AB-H.

To verify the importance of photocatalyst support for CoO<sub>x</sub> cocatalyst, a SiO<sub>2</sub>/CoO<sub>x</sub> catalyst was prepared under the same conditions as AB-Co. The preparation procedure is described in supporting information. The photothermocatalytic activity of SiO<sub>2</sub>/CoO<sub>x</sub> was tested and compared with AB-Co. As can be seen in Fig. 6, the CH<sub>4</sub> yield over AB-Co is far higher than SiO<sub>2</sub>/CoO<sub>x</sub>, indicating the irreplaceable role of TiO<sub>2</sub> support. Therefore, a synergy clearly exists between photocatalysis and thermocatalysis over AB-Co in CO<sub>2</sub> reduction, especially for the CH<sub>4</sub> production. The synergy solely benefits from CoO<sub>x</sub> grafting, indicating that the CoO<sub>x</sub> cocatalyst is a promising candidate to promote photothermocatalytic reduction of CO<sub>2</sub>.

To further evaluate the effect of CoO<sub>x</sub> dispersion on AB nanotubes, AB-Co sample was calcinated in air or N<sub>2</sub>/H<sub>2</sub>. Fig. 5d shows that calcination generally results in decreased activity over AB-Co. In detail, calcination in air leads to a simultaneously decreased production rate of CO and CH<sub>4</sub>, and whereas calcination in N<sub>2</sub>/H<sub>2</sub> selectively decreases the production rate of CH<sub>4</sub>. Note that the calcination of AB-Co affects the production of CH<sub>4</sub> more significantly than that of CO. Upon calcination, CoO<sub>x</sub> nanoparticles dispersed on AB nanotubes are believed to tend to aggregate and be of larger size, which is observed in HRTEM image in Fig. 1g and h. Therefore, it can be deduced that the high dispersion of CoO<sub>x</sub> nanoparticles is essential in promoting photothermocatalytic reduction of CO<sub>2</sub>. The higher dispersion of grafted CoO<sub>x</sub> cocatalyst, the higher yield of CH<sub>4</sub> products.

#### 3.4.4. The synergistic effect of oxygen vacancy and CoO<sub>x</sub> on photothermocatalytic reduction of CO<sub>2</sub>

As confirmed in aforementioned results, the introduced oxygen vacancy on AB nanotubes helps further dispersion of grafted CoO<sub>x</sub>. When the loading is held constant among all the CoO<sub>x</sub> grafted samples, the highest dispersion of CoO<sub>x</sub> in AB-H-Co results in the smallest size of CoO<sub>x</sub>. The size of CoO<sub>x</sub> is too small to be observed by HRTEM, suggesting that CoO<sub>x</sub> is monodispersed or even single-atom dispersed on the surface of the AB nanotubes. Fig. 7a and Table 1 compare the activities and selectivity of the photocatalytic and photothermocatalytic reduction of CO<sub>2</sub> over all samples. Sample AB-H-Co displays the champion value in the evolution of both CO and CH<sub>4</sub> products. The production rate of CH<sub>4</sub> is even 3.1 times higher than the sum of AB-H and AB-Co, confirming that an obvious synergy exists between the oxygen vacancy and the CoO<sub>x</sub> cocatalyst. This synergy leads to an optimal dispersion of CoO<sub>x</sub> cocatalyst and small size of CoO<sub>x</sub> clusters. This leads to the highest photothermocatalytic activity of AB-H-Co. The

selectivity shows that oxygen vacancies help increase selectivity of CO and whereas CoO<sub>x</sub> helps increase selectivity of CH<sub>4</sub> in PTC test. When the CoO<sub>x</sub> and oxygen vacancies co-exist on the surface of AB nanotube, the synergistic effect between CoO<sub>x</sub> and oxygen vacancies leads to the highest selectivity of CH<sub>4</sub>, which is in consistence with its best PTC activity.

To evaluate the efficiency of the catalytic system, P25 and P25/CoO<sub>x</sub> catalyst were prepared under the same conditions as AB-H-Co. The preparation procedure is described in supporting information. As shown in Fig. 7b, for PC, all three samples produce a slight amount of CO (ca. 1 μmol/g/h). Similar to AB-H-Co, CoO<sub>x</sub> grafting on P25 leads to insignificant enhancement of photocatalytic activity. However, for PTC, the production rate of CH<sub>4</sub> over AB-H-Co is 8.82 and 3.16 times higher than reference samples of P25 and P25/CoO<sub>x</sub>, respectively. Meanwhile, sample AB-H-Co displays comparable or even higher activity than that in other works (see Table S1), indicating the as-adopted PTC strategy is promising for CO<sub>2</sub> reduction.

In combination with above results of photothermocatalytic test over six typical samples, several conclusions can be drawn as follows:

- (1) By photocatalysis, AB enables CO<sub>2</sub> reduction to CO rather than CH<sub>4</sub>. By photothermocatalysis, the catalytic activity can be greatly enhanced, but still limited to enhanced CO production.
- (2) By photocatalysis, neither the introduction of slight oxygen vacancies nor loading ultra-low amounts of CoO<sub>x</sub> cocatalyst enhance the activity of CO<sub>2</sub> reduction. By photothermocatalysis, both approaches offer enhancement. Oxygen vacancy only promotes CO production whereas CoO<sub>x</sub> cocatalyst promotes both CO and CH<sub>4</sub> production.
- (3) By photocatalysis, the synergy between oxygen vacancy and CoO<sub>x</sub> cocatalyst leads to no activity enhancement. By photothermocatalysis, this synergy drastically promotes the reduction of CO<sub>2</sub>, especially CH<sub>4</sub> production, benefiting from the optimal dispersion and smallest size of CoO<sub>x</sub> cocatalyst.

#### 3.5. Mechanism for the boosted activity of CO<sub>2</sub> reduction over photothermocatalyst

It is essential to first study the role of oxygen vacancy and CoO<sub>x</sub> to understand the photothermocatalytic process of CO<sub>2</sub> reduction. Most research has focused on boosting CO<sub>2</sub> reduction via the introduction of oxygen vacancy. On one hand, the oxygen vacancy can decrease the adsorption and activation energy of CO<sub>2</sub>. For example, STM studies have shown that CO<sub>2</sub> preferentially adsorbs on oxygen vacancy sites of TiO<sub>2</sub>. The energy barrier for CO<sub>2</sub> hopping into an oxygen vacancy is 0.09 eV, which is much lower than 0.16 eV for CO<sub>2</sub> hopping out an

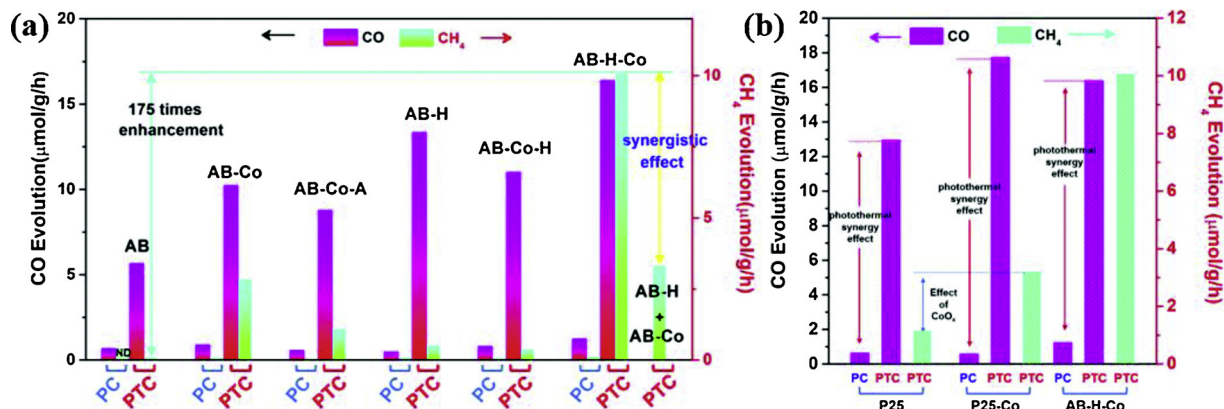


Fig. 7. a: Photocatalytic and photothermocatalytic induced CO<sub>2</sub> conversion over different samples; b: Histograms of catalytic production of CO and CH<sub>4</sub> over P25, P25-Co and AB-H-Co. PC stands for photocatalysis and PTC stands for photothermocatalysis. ND = not detected.

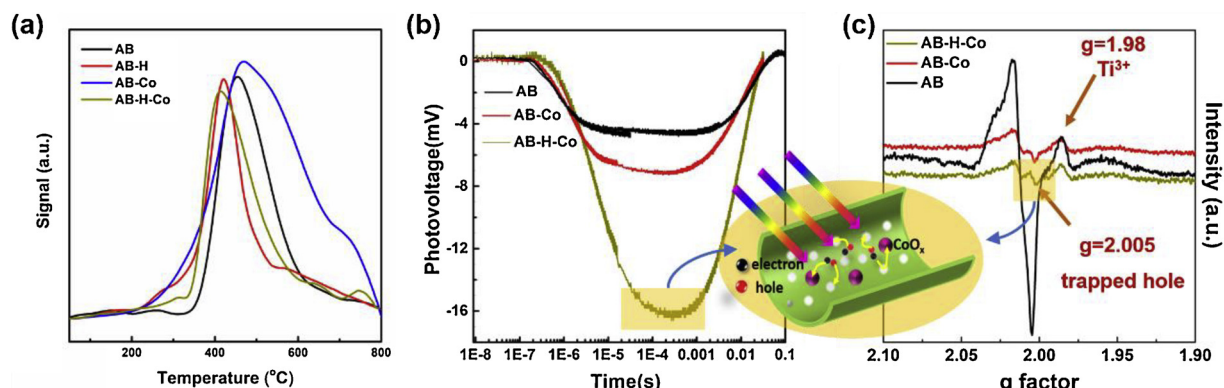


Fig. 8. (a): O<sub>2</sub>-TPD profiles of AB, AB-H, AB-Co, and AB-H-Co; (b): Transient photovoltage responses of AB, AB-Co, and AB-H-Co. The wavelength and the intensity of the laser are 355 nm and 100 μJ, respectively; (c): ESR spectra of AB, AB-Co, and AB-H-Co at 110 K with UV irradiation; inset shows a hole transfer over AB-H-Co.

oxygen vacancy [61]. The electron donating activity is increased nearby oxygen vacancies. At the oxygen vacancy defect, the initial step of CO<sub>2</sub> reduction can proceed and transient CO<sub>2</sub><sup>−</sup> is formed via a one-electron transfer. Moreover, the barrier of two-electron reduction of CO at oxygen vacancies is 0.06 eV lower than the perfect TiO<sub>2</sub> [62,63]. On the other hand, the oxygen vacancy formed on the surface or sub-surface of TiO<sub>2</sub> is advantageous for electron trapping, which is beneficial for charge separation. In the point of thermocatalytic view, O<sub>2</sub>-TPD was performed to understand the role of oxygen vacancies. Fig. 8a shows that obvious oxygen desorption can be observed in the temperature range of 300–600 °C. As reported in the literatures, the desorption peaks in this range originate from desorption of subsurface lattice oxygen [64]. The temperature at peak maximum follows the sequence of AB-H-Co ~ AB-H < AB < AB-Co. Accordingly, the introduction of oxygen vacancy helps activate the lattice oxygen, and CoO<sub>x</sub> enhanced the adsorption of the catalysts to oxygen. In fact, tremendous researches on thermocatalytic conversion of CO<sub>2</sub> have witnessed that oxygen vacancies are essential for endowing catalyst excellent ability of coke resistance [65]. This ensures a chemical looping reduction of CO<sub>2</sub> and high catalytic activity during the whole process. In this work, the as-observed lower activation temperature of lattice oxygen in sample AB-H-Co may inhibit carbon deposition. Moreover, the photothermal synergy could further facilitate the proton coupled reduction of carbon intermediate. Taking consideration of well-reported and consistent results on the positive role of oxygen vacancy for CO<sub>2</sub> reduction from viewpoint of thermodynamics, we believe that the advantages of oxygen vacancy played in photocatalysis are also applicable in photothermocatalysis.

To understand the role of CoO<sub>x</sub> cocatalyst in CO<sub>2</sub> reduction, transient photovoltage spectra is required (Fig. 8b). At the time scale of

10<sup>−8</sup> to 10<sup>−7</sup> s, the photovoltages remain positive over all the samples, which is inconsistent with the nature of an n-type semiconductor. From 10<sup>−7</sup> to 10<sup>−4</sup> s, the photovoltage gradually changes from positive to negative, and the peak-valley value of photovoltage varies from each other. The value for AB-H-Co is the most negative, followed by AB-Co, and then AB. As is previously reported, the photovoltage response at this stage mainly reflects competition between diffusion and recombination of photogenerated electrons and holes [60,66,67]. During the diffusion process, there is a higher transfer rate of electrons, which usually leads to an accumulation of more electrons than holes, due to the lower effective mass of electron than a hole. Here, the consistent inverse of photovoltage response of all the samples agrees with this rule. Electron diffusion is accompanied by recombination with holes. When the recombination is inhibited by hole trapping, then the photovoltage is more negative and lasts for a longer time. In terms of the different responses of AB, AB-Co, and AB-H-Co, it is inferred that grafted CoO<sub>x</sub> acts as a hole trap. Moreover, grafted CoO<sub>x</sub> on AB-H works better for charge separation than that on AB. This inhibition of charge recombination by trapping holes around the surface CoO<sub>x</sub> is conductive not only to the accumulation of electrons for multi-electron transfer but also oxidation of water for multi-proton release. Thus, the photothermocatalytic activity enhanced by CoO<sub>x</sub> catalyst is closely correlated with its role in hole transfer from AB nanotube.

To further evident the effect of hole trapping by CoO<sub>x</sub>, ESR spectra were collected over AB, AB-H, AB-Co, AB-H-Co and shown in Fig. 8c. In general, the ESR signals over irradiated TiO<sub>2</sub> at a lower temperature (< 150 K) display two features. One feature is located at g<sub>⊥</sub> = 1.99–1.97, which is assigned to trapped electrons in terms of Ti<sup>3+</sup>. The other feature is located at g = 2.002–2.030, which is assigned to trapped holes and superimposed oxygen species of O<sup>−</sup> and O<sub>2</sub><sup>−</sup>. For

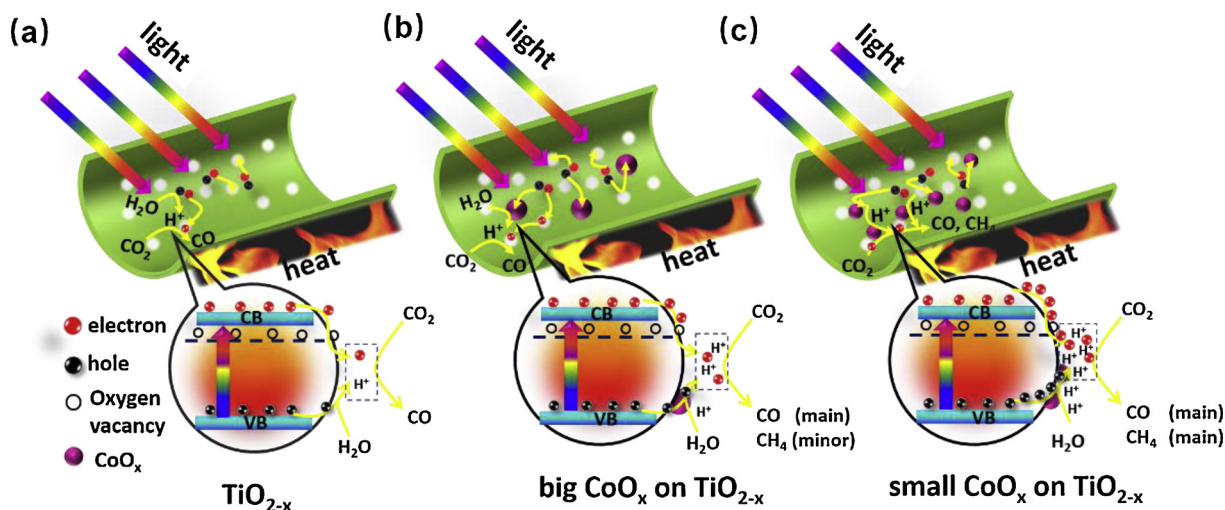


Fig. 9. Scheme of photothermocatalytic reaction over three typical samples: (a):  $\text{TiO}_{2-x}$ ; (b): big  $\text{CoO}_x$  clusters modified  $\text{TiO}_{2-x}$ ; and (c): small  $\text{CoO}_x$  clusters modified  $\text{TiO}_{2-x}$ .

sample AB, strong signals can be observed in the region of  $g = 2.00-2.03$ . After  $\text{CoO}_x$  grafting, there is no obvious decrease in signal intensity at  $g = 1.99$ , indicating that grafting of  $\text{CoO}_x$  could not interrupt the trapping of photogenerated electrons. Conversely, the initially strong signals over AB obviously decrease after  $\text{CoO}_x$  grafting, which can be observed in both AB-Co and AB-H-Co. Since the trapping of electrons is not interrupted, the decrease in signals is mainly related to the inhibition of  $\text{O}^-$  species. As is well documented, the  $\text{O}^-$  species are formed via the reaction of holes with surface bridging oxygen atoms or lattice oxygen atoms, hence the decrease of the signal of  $\text{O}^-$  species means decreased holes on  $\text{TiO}_2$ . This decrease of holes suggests a transfer of holes from  $\text{TiO}_2$  to  $\text{CoO}_x$ . Meanwhile, on a closer inspection of spectra in the region of  $g = 2.00-2.03$ , an additional signal appears at  $g = 2.005$ . As demonstrated by Nosaka and others, trapped holes give the characteristic signal at  $g = 2.005$  [68]. Thus, the additional signal at  $g = 2.005$  likely results from the trapped holes due to the presence of a  $\text{CoO}_x$  site. In combination with the decreased signal of  $\text{O}^-$  species around  $\text{TiO}_2$  and trapped holes, we conclude that grafting of  $\text{CoO}_x$  plays an important role in extracting holes from  $\text{TiO}_2$ .

Fig. 9 illustrates the mechanism of photothermocatalytic reduction of  $\text{CO}_2$  over the  $\text{TiO}_{2-x}/\text{CoO}_x$ .  $\text{CO}_2$  is initially adsorbed by the oxygen vacancy on the surface of the nanotube. Upon excitation by UV light, the photogenerated electrons tend to be trapped by oxygen vacancies and transfer to adsorbed  $\text{CO}_2$ , as shown in Fig. 9a. Meanwhile, the photogenerated holes tend to be trapped by surface  $\text{CoO}_x$  cocatalysts. Oxidation of  $\text{H}_2\text{O}$  proceeds at  $\text{CoO}_x$  site and the proton is released, as shown in Fig. 9b. To access  $\text{CO}_2$  reduction, electron transfer and proton transfer is expected to be synchronous. Since the time scale for electron transfer and proton transfer stays on picosecond and hundreds of microseconds, the rate determining step is proton transfer process. The imposed thermal radiation leads to enhanced proton transfer. This benefits multiple proton/electron coupling. Moreover, in comparison with other  $\text{CoO}_x$  modified AB samples, the smaller size of  $\text{CoO}_x$  allows quicker transfer of trapped holes to  $\text{H}_2\text{O}$ , producing more protons for  $\text{CO}_2$  reduction, as shown in Fig. 9c. Therefore, the photothermocatalytic activity is superior to other AB samples modified by larger sized  $\text{CoO}_x$ .

#### 4. Conclusion

In summary, we have developed an efficient photothermocatalyst by modifying  $\text{TiO}_2$  nanotube with slight oxygen vacancies and ultralow amount of  $\text{CoO}_x$ . Its photothermocatalytic activity in terms of  $\text{CH}_4$  evolution is 111 times higher than single photocatalysis and 175 times higher than that of pristine  $\text{TiO}_2$ . Comprehensive analysis reveals that

the introduction of oxygen vacancies is beneficial for the charge separation and dispersion of  $\text{CoO}_x$  cocatalyst, and the grafted  $\text{CoO}_x$  acts as a hole trap and promotes the release of more protons. Thus, there is more opportunity for provided for  $\text{CH}_4$  production after grafting  $\text{CoO}_x$  cocatalyst around the oxygen vacancies. This work presents a different insight by comparing photothermocatalysis and photocatalysis. It offers a novel route for the design of highly efficient photothermocatalysts towards  $\text{CO}_2$  reduction.

#### Acknowledgments

This work was supported by the Natural Science Foundation of China (Grant Nos. 51072032 and 51102001), the Key Project of Chinese Ministry of Education (No 113020A), the 111 project (No. B13013), China Postdoctoral Science Foundation (2014M551156), Jilin Province Science and Technology Development Project (20180101175JC, 20160520170JHH) and Jilin Provincial Education Department Project (No. 52, 2016). This research was partially supported by the U.S. Department of Energy (DOE), Office of Science, Office of Basic Energy Sciences, Early Career Research program under Award #67037.

#### Appendix A. Supplementary data

Supplementary material related to this article can be found, in the online version, at doi:<https://doi.org/10.1016/j.apcatb.2018.11.022>.

#### References

- [1] W. Kim, E. Edri, H. Frei, Hierarchical inorganic assemblies for artificial photosynthesis, *Acc. Chem. Res.* 49 (2016) 1634–1645.
- [2] D. Gust, Thomas A. Moore, Ana L. Moore, Solar fuels via artificial photosynthesis, *Acc. Chem. Res.* 42 (2009) 1890–1898.
- [3] A. Listorti, J. Durrant, J. Barber, Artificial photosynthesis: solar to fuel, *Nat. Mater.* 8 (2009) 929–930.
- [4] R.J. Detz, J.N.H. Reek, B.C.C. van der Zwaan, The future of solar fuels: when could they become competitive? *Energy Environ. Sci.* 11 (2018) 1653–1669, <https://doi.org/10.1039/c8ee00111a>.
- [5] Y. Wang, J. Zhao, Y. Li, C. Wang, Selective photocatalytic  $\text{CO}_2$  reduction to  $\text{CH}_4$  over  $\text{Pt}/\text{In}_2\text{O}_3$ : significant role of hydrogen adatom, *Appl. Catal. B: Environ.* 226 (2018) 544–553.
- [6] W. Tu, Y. Zhou, Z. Zou, Photocatalytic conversion of  $\text{CO}_2$  into renewable hydrocarbon fuels: state-of-the-art accomplishment, challenges, and prospects, *Adv. Mater.* 26 (2014) 4607–4626.
- [7] X. Chang, T. Wang, J. Gong,  $\text{CO}_2$  photo-reduction: insights into  $\text{CO}_2$  activation and reaction on surfaces of photocatalysts, *Energy Environ. Sci.* 9 (2016) 2177–2196.
- [8] W. Zhang, L. Wang, K. Wang, M.U. Khan, M. Wang, H. Li, J. Zeng, Integration of photothermal effect and heat insulation to efficiently reduce reaction temperature

of CO<sub>2</sub> hydrogenation, *Small* 13 (2017) 201602583.

[9] G.K. Li Zhang, Yaping Meng, Jinshu Tian, Lijie Zhang, Shaolong Wan, Jingdong Lin, Yong Wang, Direct coupling of thermo- and photocatalysis for conversion of CO<sub>2</sub>–H<sub>2</sub>O into fuels, *ChemSusChem* 10 (2017) 4709–4714.

[10] L. Wang, Y. Wang, Y. Cheng, Z. Liu, Q. Guo, M.N. Ha, Z. Zhao, Hydrogen-treated mesoporous WO<sub>3</sub> as a reducing agent of CO<sub>2</sub> to fuels (CH<sub>4</sub> and CH<sub>3</sub>OH) with enhanced photothermal catalytic performance, *J. Mater. Chem. A* 4 (2016) 5314–5322.

[11] B. Liu, X. Zhao, C. Terashima, A. Fujishima, K. Nakata, Thermodynamic and kinetic analysis of heterogeneous photocatalysis for semiconductor systems, *Phys. Chem. Chem. Phys.* 16 (2014) 8751–8760.

[12] G. Chen, R. Gao, Y. Zhao, Z. Li, G.I.N. Waterhouse, R. Shi, J. Zhao, M. Zhang, L. Shang, G. Sheng, X. Zhang, X. Wen, L.Z. Wu, C.H. Tung, T. Zhang, Alumina-supported CoFe alloy catalysts derived from layered-double-hydroxide nanosheets for efficient photothermal CO<sub>2</sub> hydrogenation to hydrocarbons, *Adv. Mater.* 30 (2018) 1704663.

[13] I.L. Leites, D.A. Sama, N. Lior, The theory and practice of energy saving in the chemical industry: some methods for reducing thermodynamic irreversibility in chemical technology processes, *Energy* 28 (2003) 55–97.

[14] M.N. Ha, G. Lu, Z. Liu, L. Wang, Z. Zhao, 3DOM-LaSrCoFeO<sub>6</sub>–δ as a highly active catalyst for the thermal and photothermal reduction of CO<sub>2</sub> with H<sub>2</sub>O to CH<sub>4</sub>, *J. Mater. Chem. A* 4 (2016) 13155–13165.

[15] M. Xing, Y. Zhou, C. Dong, L. Cai, L. Zeng, B. Shen, L. Pan, C. Dong, Y. Chai, J. Zhang, Y. Yin, Modulation of the reduction potential of TiO<sub>2-x</sub> by fluorination for efficient and selective CH<sub>4</sub> generation from CO<sub>2</sub> photoreduction, *Nano Lett.* 18 (2018) 3384–3390.

[16] J. Jiao, Y. Wei, Y. Zhao, Z. Zhao, A. Duan, J. Liu, Y. Pang, J. Li, G. Jiang, Y. Wang, AuPd/3DOM-TiO<sub>2</sub> catalysts for photocatalytic reduction of CO<sub>2</sub>: high efficient separation of photogenerated charge carriers, *Appl. Catal. B: Environ.* 209 (2017) 228–239.

[17] Y. Zhao, Y. Wei, X. Wu, H. Zheng, Z. Zhao, J. Liu, J. Li, Graphene-wrapped Pt/TiO<sub>2</sub> photocatalysts with enhanced photogenerated charges separation and reactant adsorption for high selective photoreduction of CO<sub>2</sub> to CH<sub>4</sub>, *Appl. Catal. B: Environ.* 226 (2018) 360–372.

[18] X. Li, J. Wen, J. Low, Y. Fang, J. Yu, Design and fabrication of semiconductor photocatalyst for photocatalytic reduction of CO<sub>2</sub> to solar fuel, *Sci. China Mater.* 57 (2014) 70–100.

[19] A. Iwase, S. Yoshino, T. Takayama, Y.H. Ng, R. Amal, A. Kudo, Water splitting and CO<sub>2</sub> reduction under visible light irradiation using Z-scheme systems consisting of metal sulfides, CoO<sub>x</sub>-loaded BiVO<sub>4</sub>, and a reduced graphene oxide electron mediator, *J. Am. Chem. Soc.* 138 (2016) 10260–10264.

[20] J. Tang, J.R. Durrant, David R. Klug, Mechanism of photocatalytic water splitting in TiO<sub>2</sub>: Reaction of water with photoholes, importance of charge carrier dynamics, and evidence for four-hole chemistry, *J. Am. Chem. Soc.* 130 (2008) 13885–13891.

[21] J. Chen, Y.F. Li, P. Sit, A. Selloni, Chemical dynamics of the first proton-coupled electron transfer of water oxidation on TiO<sub>2</sub> anatase, *J. Am. Chem. Soc.* 135 (2013) 18774–18777.

[22] O.K. Varghese, M. Paulose, T.J. LaTempa, C.A. Grimes, High-rate solar photocatalytic conversion of CO<sub>2</sub> and water vapor to hydrocarbon fuels, *Nano Lett.* 9 (2009) 731–737.

[23] A. Dhakshinamoorthy, S. Navalon, A. Corma, H. Garcia, Photocatalytic CO<sub>2</sub> reduction by TiO<sub>2</sub> and related titanium containing solids, *Energy Environ. Sci.* 5 (2012) 9217–9233.

[24] X. Li, Z. Zhuang, W. Li, H. Pan, Photocatalytic reduction of CO<sub>2</sub> over noble metal-loaded and nitrogen-doped mesoporous TiO<sub>2</sub>, *Appl. Catal. A: Gen.* 429–430 (2012) 31–38.

[25] S. Xie, Y. Wang, Q. Zhang, W. Deng, Y. Wang, MgO- and Pt-promoted TiO<sub>2</sub> as an efficient photocatalyst for the preferential reduction of carbon dioxide in the presence of water, *ACS Catal.* 4 (2014) 3644–3653.

[26] S.N. Habreutinger, L. Schmidt-Mende, K.J. Stolarczyk, Photocatalytic reduction of CO<sub>2</sub> on TiO<sub>2</sub> and other semiconductors, *Angew. Chem. Int. Ed.* 52 (2013) 7372–7408.

[27] X. Qiu, M. Miyachi, K. Sunada, M. Minoshima, M. Liu, Y. Lu, D. Li, Y. Shimodaira, Y. Hosogi, Y. Kuroda, K. Hashimoto, Hybrid Cu<sub>x</sub>O/TiO<sub>2</sub> nanocomposites as risk-reduction materials in indoor environments, *ACS Nano* 6 (2012) 1609–1618.

[28] M. Liu, X. Qiu, M. Miyachi, K. Hashimoto, Energy-level matching of Fe(III) ions grafted at surface and doped in bulk for efficient visible-light photocatalysts, *J. Am. Chem. Soc.* 135 (2013) 10064–10072.

[29] A.K.P.D. Savio, J. Fletcher, K. Smith, R. Iyer, J.M. Bao, F.C. Robles Hernández, Environmentally effective photocatalyst CoO–TiO<sub>2</sub> synthesized by thermal precipitation of Co in amorphous TiO<sub>2</sub>, *Appl. Catal. B: Environ.* 182 (2016) 449–455.

[30] L. Kong, C. Wang, F. Wan, H. Zheng, X. Zhang, Synergistic effect of surface self-doping and Fe species-grafting for enhanced photocatalytic activity of TiO<sub>2</sub> under visible-light, *Appl. Surf. Sci.* 396 (2017) 26–35.

[31] C. Wang, X. Zhang, Y. Liu, Promotion of multi-electron transfer for enhanced photocatalysis: a review focused on oxygen reduction reaction, *Appl. Surf. Sci.* 358 (2015) 28–45.

[32] A. Yamakata, M. Kawaguchi, N. Nishimura, T. Minegishi, J. Kubota, K. Domen, Behavior and energy states of photogenerated charge carriers on Pt- or CoO<sub>x</sub>-loaded LaTiO<sub>2</sub>N photocatalysts: time-resolved visible to mid-infrared absorption study, *J. Phys. Chem. C* 118 (2014) 23897–23906.

[33] S.S. Gujral, A.N. Simonov, M. Higashi, X.-Y. Fang, R. Abe, L. Spiccia, Highly dispersed cobalt oxide on TaON as efficient photoanodes for long-term solar water splitting, *ACS Catal.* 6 (2016) 3404–3417.

[34] Z. Chen, Z. Duan, Z. Wang, X. Liu, L. Gu, F. Zhang, M. Dupuis, C. Li, Amorphous cobalt oxide nanoparticles as active water-oxidation catalysts, *ChemCatChem* 9 (2017) 3641–3645.

[35] X. Huang, G. Zhao, G. Wang, Sub-nano CoO<sub>x</sub> attached onto WO<sub>3</sub> for efficient photocatalytic and photoelectrochemical water oxidation, *J. Mater. Chem. A* 5 (2017) 24631–24635.

[36] J. Zhang, Z. Yu, Z. Gao, H. Ge, S. Zhao, C. Chen, S. Chen, X. Tong, M. Wang, Z. Zheng, Y. Qin, Porous TiO<sub>2</sub> nanotubes with spatially separated platinum and CoO<sub>x</sub> cocatalysts produced by atomic layer deposition for photocatalytic hydrogen production, *Angew. Chem. Int. Ed.* 56 (2017) 816–820.

[37] Z. Sun, J.M.T.A. Fischer, Q. Li, J. Hu, Q. Tang, H. Wang, Z. Wu, M. Hankel, D.J. Searles, L. Wang, Enhanced CO<sub>2</sub> photocatalytic reduction on alkali-decorated graphitic carbon nitride, *Appl. Catal. B: Environ.* 216 (2017) 146–155.

[38] C. Dong, C. Lian, S. Hu, Z. Deng, J. Gong, M. Li, H. Liu, M. Xing, J. Zhang, Size-dependent activity and selectivity of carbon dioxide photocatalytic reduction over platinum nanoparticles, *Nat. Commun.* 9 (2018) 1252.

[39] Y. Ji, Y. Luo, New mechanism for photocatalytic reduction of CO<sub>2</sub> on the anatase TiO<sub>2</sub>(101) surface: the essential role of oxygen vacancy, *J. Am. Chem. Soc.* 138 (2016) 15896–15902.

[40] T. Billo, F.Y. Fu, P. Raghunath, I. Shown, W.F. Chen, H.T. Lien, T.H. Shen, J.F. Lee, T.S. Chan, K.Y. Huang, C.I. Wu, M.C. Lin, J.S. Hwang, C.H. Lee, L.C. Chen, K.H. Chen, Ni-nanocluster modified black TiO<sub>2</sub> with dual active sites for selective photocatalytic CO<sub>2</sub> reduction, *Small* 14 (2018) 1702928.

[41] M. Liu, Y. Chen, T. Lin, C. Mou, Defective mesocrystal ZnO-supported gold catalysts: facilitating CO oxidation via vacancy defects in ZnO, *ACS Catal.* 8 (2018) 6862–6869.

[42] C. Wang, X. Zhang, Y. Wei, L. Kong, F. Chang, H. Zheng, L. Wu, J. Zhi, Y. Liu, Correlation between band alignment and enhanced photocatalysis: a case study with anatase/TiO<sub>2</sub>(B) nanotube heterojunction, *Dalton Trans.* 44 (2015) 13331–13339.

[43] C. Wang, X. Zhang, Y. Zhang, Y. Jia, J. Yang, P. Sun, Y. Liu, Hydrothermal growth of layered titanate nanosheet arrays on titanium foil and their topotactic transformation to heterostructured TiO<sub>2</sub> photocatalysts, *J. Phys. Chem. C* 115 (2011) 22276–22285.

[44] C. Wang, X. Zhang, Y. Liu, Coexistence of an anatase/TiO<sub>2</sub>(B) heterojunction and an exposed (001) facet in TiO<sub>2</sub> nanoribbon photocatalysts synthesized via a fluorine-free route and topotactic transformation, *Nanoscale* 6 (2014) 5329–5337.

[45] X. Chen, L. Liu, P.Y. Yu, S.S. Mao, Increasing solar absorption for photocatalysis with black hydrogenated titanium dioxide nanocrystals, *Science* 331 (2011) 746–750.

[46] S. Neubert, D. Mitoraj, S.A. Shevlin, P. Pulisova, M. Heimann, Y. Du, G.K.L. Goh, M. Pacia, K. Kruczala, S. Turner, W. Macyk, Z.X. Guo, R.K. Hocking, R. Beranek, Highly efficient rutile TiO<sub>2</sub> photocatalysts with single Cu(II) and Fe(III) surface catalytic sites, *J. Mater. Chem. A* 4 (2016) 3127–3138.

[47] T. Ohsaka, F. Izumi, Y. Fujiki, Raman spectrum of anatase, TiO<sub>2</sub>, *J. Raman Spectrosc.* 7 (1978) 321–324.

[48] H. Lin, X. Wang, Epitaxy of radial high-energy-faceted ultrathin TiO<sub>2</sub> nanosheets onto nanowires for enhanced photoreactivities, *Adv. Funct. Mater.* 26 (2016) 1580–1589.

[49] A. Naldoni, M. Alietta, S. Santangelo, M. Marelli, F. Fabbri, S. Cappelli, C.L. Bianchi, R. Psaro, V. Dal Santo, Effect of nature and location of defects on bandgap narrowing in black TiO<sub>2</sub> nanoparticles, *J. Am. Chem. Soc.* 134 (2012) 7600–7603.

[50] G. Yin, Q. Bi, W. Zhao, J. Xu, T. Lin, F. Huang, Efficient conversion of CO<sub>2</sub> to methane photocatalyzed by conductive black titania, *ChemCatChem* 9 (2017) 4389–4396.

[51] L. Huang, J. Jiang, L. Ai, Interlayer expansion of layered cobalt hydroxide nanobelts to highly improve oxygen evolution electrocatalysis, *ACS Appl. Mater. Interfaces* 9 (2017) 7059–7067.

[52] J. Huo, Y. Hu, H. Jiang, C. Li, In situ surface hydrogenation synthesis of Ti<sup>3+</sup> self-doped TiO<sub>2</sub> with enhanced visible light photoactivity, *Nanoscale* 6 (2014) 9078–9084.

[53] T. Leshuk, R. Parviz, P. Everett, H. Krishnakumar, R.A. Varin, F. Gu, Photocatalytic activity of hydrogenated TiO<sub>2</sub>, *ACS Appl. Mater. Interfaces* 5 (2013) 1892–1895.

[54] G. Zhang, L. Qin, L. Chen, Z. Xu, M. Liu, X. Guo, One-pot synthesis of mesoporous anatase-TiO<sub>2</sub>(B) mixed-phase nanowires decorated with sulfur and Fe<sub>2</sub>O<sub>3</sub> nanoparticles for visible-light photochemical oxidation, *ChemCatChem* 8 (2016) 426–433.

[55] H. Liu, B. Lin, L. He, H. Qu, P. Sun, B. Gao, Y. Chen, Mesoporous cobalt-intercalated layered titanate for efficient visible-light photocatalysis, *Chem. Eng. J.* 215–216 (2013) 396–403.

[56] K. Li, D. Xue, Estimation of electronegativity values of elements in different valence states, *J. Phys. Chem. A* 110 (2006) 11332–11337.

[57] R. Sanjinés, H. Tang, H. Berger, F. Gozzo, G. Margaritondo, F. Lévy, Electronic structure of anatase TiO<sub>2</sub> oxide, *J. Appl. Phys.* 75 (1994) 2945–2951.

[58] H. Shibata, Y. Ogura, Y. Sawa, Y. Kono, Hydroxyl radical generation depending on O<sub>2</sub> or H<sub>2</sub>O by a photocatalyzed reaction in an aqueous suspension of titanium dioxide, *Biosci., Biotech., Biochem.* 62 (2014) 2306–2311.

[59] J.O. Nriagu, Mechanistic steps in the photoreduction of mercury in natural waters, *Sci. Total Environ.* 154 (1994) 1–8.

[60] H. Zheng, C. Wang, X. Zhang, Y. Li, H. Ma, Y. Li, u, Control over energy level match in Keggin polyoxometallate-TiO<sub>2</sub> microspheres for multielectron photocatalytic reactions, *Appl. Catal. B: Environ.* 234 (2018) 79–89.

[61] X. Lin, Z.T. Wang, Y. Lyubinetsky, B.D. Kay, Z. Dohnalek, Interaction of CO<sub>2</sub> with oxygen adatoms on rutile TiO<sub>2</sub>(110), *Phys. Chem. Chem. Phys.* 15 (2013) 6190–6195.

[62] T. Wang, X. Meng, P. Li, S. Ouyang, K. Chang, G. Liu, Z. Mei, J. Ye, Photoreduction of CO<sub>2</sub> over the well-crystallized ordered mesoporous TiO<sub>2</sub> with the confined space effect, *Nano Energy* 9 (2014) 50–60.

[63] X. Meng, S. Ouyang, T. Kako, P. Li, Q. Yu, T. Wang, J. Ye, Photocatalytic CO<sub>2</sub> conversion over alkali modified TiO<sub>2</sub> without loading noble metal cocatalyst, *Chem. Commun.* 50 (2014) 11517–11519.

[64] J. Li, E. Yu, S. Cai, X. Chen, J. Chen, H. Jia, Y. Xu, Noble metal free, CeO<sub>2</sub>/LaMnO<sub>3</sub> hybrid achieving efficient photo-thermal catalytic decomposition of volatile organic compounds under IR light, *Appl. Catal. B: Environ.* 240 (2019) 141–152.

[65] I. Luisetto, S. Tuti, C. Battocchio, S. Mastro, A. Sodo, Ni/CeO<sub>2</sub>–Al<sub>2</sub>O<sub>3</sub> catalysts for the dry reforming of methane: the effect of CeAlO<sub>3</sub> content and nickel crystallite size on catalytic activity and coke resistance, *Appl. Catal. A: Gen.* 500 (2015) 12–22.

[66] L. Zhang, S. Li, B. Liu, D. Wang, T. Xie, Highly efficient CdS/WO<sub>3</sub> photocatalysts: Z-scheme photocatalytic mechanism for their enhanced photocatalytic H<sub>2</sub> evolution under visible light, *ACS Catal.* 4 (2014) 3724–3729.

[67] Y. Liu, Y. Lin, T. Xie, L. Chen, S. Yi, D. Wang, Effect of photogenerated charge transfer on the photocatalysis in high-performance hybrid Pt-Co:ZnO nanostructure photocatalyst, *ACS Appl. Mater. Interfaces* 5 (2013) 4017–4020.

[68] Y. Nosaka, S. Takahashi, H. Sakamoto, A.Y. Nosaka, Reaction mechanism of Cu(II)-grafted visible-light responsive TiO<sub>2</sub> and WO<sub>3</sub> photocatalysts studied by means of ESR spectroscopy and chemiluminescence photometry, *J. Phys. Chem. C* 115 (2011) 21283–21290.